Research Square

Preprints are preliminary reports that have not undergone peer review.
They should not be considered conclusive, used to inform clinical practice,
or referenced by the media as validated information.

Erbium-Intercalated V2C MXene as a Sunlight-Responsive Photocatalyst for Degradation of sulfamethoxazole antibiotic and Rhodamine B dye with Potential Toxicity Towards Cancer Cells

Mahvish Fatima
M.AZIZ@qu.edu.sa

Qassim University
Majid Ali
Xi'an Jiaotong University
Shamaila Fatima
Shanghai University
Attalla F El-kott
King Khalid University
Mohammed A. AlShehri
King Khalid University
Eman A Al-Shahari
King Khalid University
Muhammad Hammad Aziz
COMSATS University Islamabad
Alisher Abduvokhidov
Andijan State University

Research Article

Keywords: Photocatalysis, MXene, Intercalation, redox modulation, anticancer

Posted Date: July 17th, 2026

DOI: https://doi.org/10.21203/rs.3.rs-10302485/v1

License: This work is licensed under a Creative Commons Attribution 4.0 International License. Read Full License

Additional Declarations: No competing interests reported.

Abstract

Engineering the electronic structure of MXenes through rare-earth intercalation offers a promising route to regulate their redox activity and multifunctional performance. Herein, we report the synthesis of erbium-intercalated V_2C MXene (Er@V_2C) as a sunlight-responsive nanoplatform for environmental remediation and biomedical applications. Structural analysis confirmed successful Al removal from the V_2AlC MAX phase and subsequent interlayer expansion upon Er^{3+} intercalation, with the (002) diffraction peak shifting from 13.4° to 9.1° and further to 8.9°, corresponding to an increased c-lattice parameter of 19.86 Å. Optical studies revealed band-gap narrowing from 2.21 to 1.98 eV which indicated the enhanced visible-light absorption. Raman and FTIR analyses demonstrated lattice distortion and modified surface terminations while BET measurements showed mesoporous architecture with a surface area of 90 m^2g^{-1} that reflecting suppressed nanosheet restacking. Under natural sunlight irradiation, Er@V_2C exhibited efficient photocatalytic degradation of Rhodamine B (82.6%) and sulfamethoxazole (90.2%) within 120 min, following pseudo-first-order kinetics. The catalyst also showed excellent stability over repeated cycles. Beyond environmental remediation, Er@V_2C demonstrated concentration-dependent antioxidant activity and selective cytotoxicity toward HeLa cancer cells while maintaining comparatively higher viability in normal HUVEC cells. These findings reveal that erbium intercalation effectively modulates charge separation, defect density, and redox behavior in V_2C MXene, enabling the integration of solar-driven photocatalysis and selective biological activity within a single multifunctional nanomaterial system. This study highlights rare-earth intercalation as a versatile strategy for designing redox-engineered MXenes for sustainable environmental and biomedical technologies.

1. Introduction

The increasing discharge of organic dyes and pharmaceutical residues into aquatic environments poses a severe threat to ecosystems and public health due to their persistence, bioaccumulation, and toxicological effects [1]. Synthetic dyes such as Rhodamine B (RhB) are widely employed in textile and printing industries and are resistant to conventional biological treatment processes, while pharmaceutical contaminants such as sulfamethoxazole (SMX), a commonly used sulfonamide antibiotic, are frequently detected in surface and wastewater streams owing to their chemical stability and incomplete removal during wastewater treatment [2, 3]. The continuous release of antibiotics is particularly alarming, as it accelerates the development of antibiotic-resistant microorganisms and disrupts aquatic life. Consequently, the development of efficient, sustainable, and sunlight-driven technologies for the degradation of both dye and pharmaceutical pollutants remains an urgent global challenge [4, 5]. Photocatalysis has emerged as a promising advanced oxidation technology for wastewater remediation due to its ability to mineralize organic contaminants into benign products using light energy [6]. However, the widespread application of conventional photocatalysts is hindered by limited visible-light absorption, rapid recombination of photogenerated charge carriers, and low quantum efficiency under solar irradiation [7]. Addressing these limitations requires the development of novel photocatalytic materials with enhanced light-harvesting capability, improved charge separation, and tunable electronic structures that can operate efficiently under natural sunlight.

In recent years, MXenes two-dimensional transition-metal carbides and nitrides [8] have attracted growing interest as photocatalysts due to their metallic conductivity, high surface area, tunable surface terminations, and broad optical absorption. Among them, V_2C MXene is particularly appealing because of its favorable electronic structure, strong light absorption, and high redox activity [9–11]. Nevertheless, pristine V_2C MXene suffers from rapid charge recombination, limited visible-light utilization, and concerns regarding uncontrolled redox activity, which restrict its photocatalytic efficiency and biological applicability [12, 13]. Rare-earth ion intercalation has recently emerged as an effective strategy to modulate the electronic structure, optical response, and redox behavior of layered materials. Rare-earth ions possess unique 4f electronic configurations that can introduce localized energy states, enhance defect density, and act as charge-carrier traps, thereby improving visible-light absorption and suppressing electron–hole recombination [14, 15]. In particular, erbium (Er^{3+}) offers distinctive advantages, including strong electronic polarization, high chemical stability, and the ability to tailor charge-transfer pathways without significantly compromising material integrity. Despite these advantages, the potential of erbium-intercalated MXenes remains largely unexplored, especially in multifunctional systems that bridge environmental and biomedical applications [16].

In addition to environmental remediation, MXene-based materials have recently gained attention in biomedical research owing to their redox activity, surface functionalization capability and interaction with biological systems. However, vanadium-based MXenes often suffer from nonspecific cytotoxicity, limiting their therapeutic applicability. Rational electronic modulation through rare-earth intercalation offers a promising route to balance reactive oxygen species (ROS) generation and antioxidant behavior, enabling selective anticancer activity while maintaining cytocompatibility toward normal cells [17–19]. Achieving such context-dependent redox behavior within a single nanomaterial remains a significant scientific challenge [20].

In this work, we report the synthesis of erbium-intercalated V_2C MXene (Er@V_2C) [21] as a multifunctional, sunlight-responsive nanoplatform for environmental and biomedical applications. The intercalation of Er^{3+} ions effectively tailors the electronic structure of V_2C MXene, resulting in enhanced visible-light absorption, band-gap narrowing, and improved charge-carrier dynamics. The photocatalytic performance of Er@V_2C was systematically evaluated for the sunlight driven degradation of Rhodamine B dye and sulfamethoxazole antibiotic, representing model dye and pharmaceutical pollutants [22]. Furthermore, the antioxidant activity and selective anticancer potential of Er@V_2C were investigated using chemical radical scavenging assays and in-vitro cytotoxicity studies against HeLa cancer cells and normal HUVEC cells. This study introduces a rare-earth-intercalated MXene system that integrates efficient sunlight driven photocatalysis with tunable biological redox activity, offering a new paradigm for multifunctional MXene design. The findings provide fundamental insights into the role of erbium intercalation in regulating charge transport, redox behavior and cancer cells selectivity, thereby expanding the functional landscape of MXenes for sustainable environmental remediation and cancer nanomedicine.

2. Materials and Methods

2.1. Materials

Vanadium aluminum carbide (V_2AlC) MAX phase powder was used as the precursor for MXene synthesis. Hydrofluoric acid (HF, 49%) and Rhodamine B (RhB) were purchased from Sigma-Aldrich, Erbium nitrate hexahydrate ($Er(NO_3)_3 \cdot 6H_2O$, 99.9%, Alfa Aesar). 2,2-diphenyl-1-picrylhydrazyl (DPPH) and ABTS (2,2'-azino-bis(3-ethylbenzothiazoline-6-sulfonic acid)), Dulbecco's Modified Eagle Medium (DMEM), fetal bovine serum (FBS), penicillin–streptomycin, MTT reagent, and dimethyl sulfoxide (DMSO) were purchased from Thermo Fisher Scientific. Human cervical cancer (HeLa, ATCC) cells and human umbilical vein endothelial cells (HUVEC, ATCC) were used as representative cancerous and normal cell lines. Sulfamethoxazole (SMX) antibiotic tablet was purchased from local pharmacy of Lahore, Pakistan. All chemicals were of analytical grade and used without further purification.

2.2. Preparation of V_2C MXene

Two-dimensional V_2CT_x MXene nanosheets were synthesized through the wet chemical etching route on V_2AlC MAX-phase powder. Protocol consisted of 15 ml of concentrated hydrofluoric acid HF (49%) was placed into a Teflon beaker, 1g of V_2AlC MAX powder was added gradually under continuous stirring to avoid splashing facilitating homogenous reaction. The stirring was left to be kept at room temperature for 45 h at controlled rotating per minute (rpm) and carefully centrifuged repeatedly with deionized water until the supernatant attained pH 6. Vacuum filtration assembly was used for filtration and then dried in a vacuum oven overnight at 45 $^{\circ}C$.

Schematic 1. Schematic representation of V_2AlC MAX etching and preparation of multilayered V2C MXene by Al etching.

2.3. Preparation of Er@V_2C MXene

Nanocomposites of MXene and erbium nitrate hexahydrate were prepared through intercalation approach employing liquid-phase sonication. A homogeneous MXene dispersion was prepared at 1 mg mL^{-1} in deionized water, followed by 30 min of stirring and 5 min of sonication. A corresponding solution of erbium nitrate hexahydrate was prepared at a concentration of 2 mg mL^{-1} in deionized water, prepared with the identical stirring and sonication conditions. By adding erbium precursor solution dropwise into the MXene dispersion under continuous stirring for 3 h, followed by 5 minutes of sonication to facilitate intercalation. The reaction mixture was washed with deionized water to eliminate the terminations that were on surface until a pH of about 6.0 was reached, and the resulting nanocomposite was separated through vacuum filtration and dried overnight under vacuum oven at 55 $^{\circ}C$.

2.4. Characterization

The structural properties of V_2AlC, V_2C and Er@V_2C were investigated by using X-ray diffraction (XRD). The surface morphology and microstructural features were examined by scanning electron microscopy (SEM). The elemental composition and purity of the samples were further analyzed by energy dispersive X-ray spectroscopy (EDX). The optical properties and absorption behavior were studied using a UV–visible spectrometer. Raman spectroscopy was utilized to analyze molecular vibrations, bonding characteristics and structural defects within V_2C and Er@V_2C composite. Specific surface area and pore size distribution were investigated by using the Brunauer–Emmett–Teller (BET) in nitrogen adsorption–desorption measurements.

2.5. Photocatalysis protocol

The photocatalytic performance of Er@V_2C MXene was evaluated using Rhodamine B (RhB) dye and sulfamethoxazole (SMX) antibiotic as model organic pollutants under natural sunlight irradiation. In a typical experiment, 100 mL of aqueous pollutant solution with an initial concentration of 10 mg L^{-1} was transferred into a quartz reaction vessel. 100 mg of Er@V_2C MXene photocatalyst was dispersed into the solution and magnetically stirred to ensure uniform suspension. Prior to sunlight exposure, the suspension was stirred in the dark for 30 min to establish adsorption–desorption equilibrium between the catalyst surface and pollutant molecules. After equilibrium was reached, the reaction mixture was exposed to sunlight under continuously stirred. At predetermined time intervals including 20, 40, 60, 80, 100 and 120 min, 3 mL aliquots were withdrawn and centrifuged to remove catalyst Er@V_2C. The residual concentration of RhB and SMX was analyzed using a UV–visible spectrophotometer by monitoring the characteristic absorption peaks of RhB in the visible region and SMX in the UV region. The degradation efficiency (%) was calculated using the equation:

$$Degradation\ \% = \frac{C_o - C_t}{C_o} \times 100$$

where C_0 and C□ were the initial and concentration at irradiation time t respectively. Kinetic analysis was performed using a pseudo-first-order model by plotting ln(C_0/C□) versus irradiation time. Reusability of the photocatalyst was assessed by recovering Er@V_2C after each cycle via centrifugation through washing with deionized water, drying and reusing under identical conditions.

2.6. MTT assay

The *in vitro* cytotoxicity of Er@V_2C MXene was evaluated against HeLa cervical cancer cells and normal HUVEC cell lines by using the standard MTT assay. Firstly, cells were cultured in Dulbecco's Modified Eagle Medium (DMEM) supplemented with 10% fetal bovine serum and 1% penicillin–streptomycin under humidified conditions at 37°C with 5% CO_2. Cells were seeded into 96-well plates at a density of 1 × 10^4 cells/well and allowed to adhere for 24 h. After incubation, the culture medium was replaced with fresh medium and treated by adding Er@V_2C with varying concentrations 2.5, 5, 10, 15 and 20 μg/mL. The cells were then incubated for an additional 24 h. Following treatment, 20 μL of MTT solution (5 mg mL^{-1} in PBS) was added to each well and incubated for 4 h to allow formation of purple formazan crystals. The supernatant was carefully removed, and the formed crystals were dissolved in 150 μL of dimethyl sulfoxide (DMSO). The absorbance was measured at 570 nm using a microplate reader.

$$Cell\ viability\ (\%) = \frac{A_s}{A_c} \times 100$$

where A□ represents the absorbance of treated cells and A□ is the absorbance of control cells (untreated). All experiments were performed in triplicate and results were expressed as mean ± standard deviation.

3. Result and discussion

3.1. X-ray diffraction

Figure 2a represents the X-ray diffraction (XRD) pattern of the V_2AlC MAX phase, V_2C etched MXene and Er@V_2C MXene. The diffraction pattern of MAX phase is in great accord with the standard JCPDS card No. 29–0101, which indicates the presence of the pure MAX phase structure with no visible intermetallic impurities. The XRD pattern of MAX phase demonstrated the characteristics peaks (002) and (103) at 13.4° and at 41.2° respectively. After selective etching of the aluminum layers, characteristic peak (002) showed a significant shift to lower diffraction angle of 9.1°, and the calculated c-lattice parameter of 13.2 Å indicated the interlayer spacing exfoliation. The intercalation of Er^{3+} ions led to further downshift of the (002) reflection. In Er@V_2C, (002) peak was shifted to 8.9° with c-lattice parameter 19.86 Å shows the effective intercalation of Er between V_2C MXene layers [21].

3.2. Fourier transform infrared spectroscopy

Figure 2b represents the FTIR spectra of V_2AlC, V_2C and Er@V_2C composite. The structural analysis from V_2AlC MAX phase to V_2C MXene and further to Er@V_2C MXene is clearly reflected in their FTIR features and interlayer behavior. The MAX phase shows weak and broad bands at ~ 3423 cm^{-1} and ~ 1635 cm^{-1}, attributed to adsorbed -OH and H-O-H bending, along with a characteristic V-C vibration at ~ 619 cm^{-1}, indicating a compact lattice with limited surface functionality. After Al-layer etching, V_2C MXene exhibits intensified and sharper absorption bands at ~ 3436 cm^{-1} (-OH stretching), ~ 1593 cm^{-1} (H-O-H/C = C), ~ 1383 cm^{-1} (C-F) [23], and ~

1090 cm^{-1} (C-O) [24], confirming the formation of surface terminations and interlayer opening. Upon erbium intercalation, Er@V_2C retains the MXene vibrational fingerprints but shows systematic peak shifts to ~ 3409 cm^{-1}, ~ 1583 cm^{-1}, ~ 1409 cm^{-1}, and ~ 1117 cm^{-1}, indicating strengthened interlayer interactions and electronic redistribution induced by Er^{3+} ions. These spectroscopic changes correlate with the progressive low-angle shift of the (002) XRD reflection from MAX to MXene and further in Er@V_2C, confirming successive interlayer expansion and increased c-lattice parameter without disrupting the MXene framework.

3.3. SEM and EDX analysis

The surface morphology of the samples was studied by scanning electron microscopy (SEM). Figure 3 shows the MAX-phase V_2AlC close stacked, and the etched V_2CTx showed a layered and clear exfoliated, two-dimensional, sheet-like structure, and the metallic layers of aluminum have been removed successfully [25]. After the incorporation of Er, the surface roughness of the MXene sheets is increased, and intercalation on the surfaces of the sheets are evident. The successful intercalation of Er ions is also supported by the energy-dispersive X-ray spectroscopy (EDS). Vanadium and Carbon are present as the major components of V_2CTx, as the EDS spectrum displays. F is due to the HF etching process. The presence of nitrogen is attributed to the existence of ($Er(NO_3)_3{\cdot}6H_2O$) salt, and O is associated with the termination groups on the MXene layers on the surface. There is a small residual of Al, which shows that it's not removed completely. Notably, there is a large amount of Er that indicates the successful integration of the Er within the MXene structure.

Figure 4a represents the UV-visible absorption spectra of pristine V_2C MXene and Er-intercalated V_2C MXene demonstrate broad light absorption extending from the UV into the visible region, which is characteristic of MXene-based materials. Pristine V_2C shows strong absorption mainly in the UV region, whereas Er@V_2C exhibits enhanced visible-light absorption, indicating improved light-harvesting ability after Er^{3+} ion intercalation. The optical band gaps were estimated from Tauc plots by plotting $\left(\alpha\, h\nu\right)^2$ versus photon energy, assuming a direct transition as shown in Fig. 4b. The band gap of pristine V_2C was determined to be 2.21 eV, while Er@V_2C showed a reduced band gap of 1.98 eV, suggesting band-gap narrowing upon Er intercalation. This reduction can be attributed to the introduction of interlayer electronic states and defect levels associated with Er^{3+} ions, which modify the electronic structure and facilitate easier excitation of charge carriers under visible light. Consequently, enhanced visible-light absorption and narrowed bandgap of Er@V_2C are beneficial for photocatalytic applications, enable more efficient utilization of the solar spectrum and promote improved charge carrier generation and separation which can lead to enhanced photocatalytic activity.

3.5. Raman analysis

The Raman spectra of pristine V_2C MXene and Er-intercalated V_2C MXene (Er@V_2C) provide valuable insight into their lattice vibrations and structural modifications induced by rare-earth ion intercalation as shown in Fig. 4c. For pristine V_2C, several characteristic Raman bands are observed, reflecting the vibrational modes of vanadium-carbon bonds and surface functional groups [26, 27]. The intense low-frequency band below 200 cm^{-1} is attributed to lattice vibrations involving V-C stretching and collective vibrations of the MXene layers. The prominent peak centered at 467 cm^{-1} is assigned to the in-plane vibration of V-C bonds, confirming the structural integrity of the V_2C framework. Additionally, the strong band at 722 cm^{-1} originates from symmetric V-C stretching and surface-terminated vibrations, while the higher-frequency feature at 863 cm^{-1} is associated with V-O or V-C-O related modes arising from surface terminations (-O/-OH) mostly present in MXenes.

Upon Er^{3+} ion intercalation, noticeable changes in both peak intensity and position were observed in the Raman spectrum. The Er@V_2C sample exhibits a new band at 281 cm^{-1} which may be attributed to Er-O or Er-C related vibrational modes that indicated the successful intercalation of Er ions within the interlayer spacing of V_2C. Meanwhile, the characteristic V_2C peaks at 467 cm^{-1} and 722 cm^{-1} become broader and show reduced intensity suggested the lattice distortion and weakened V-C bond symmetry caused by Er^{3+} insertion. The appearance of a weak band around 988 cm^{-1} further supported the formation of Er related bonding and modified surface chemistry. The observed peak broadening and intensity reduction in Er@V_2C indicate increased structural disorder and defect formation, which are beneficial for photocatalytic applications. These defects can act as active sites for pollutant adsorption and facilitate charge trapping thereby suppressing electron-hole recombination. Overall, the Raman results confirmed successful Er intercalation into V_2C MXene, leading to lattice distortion, modified vibrational behavior and enhanced defect density which collectively contribute to the improved photocatalytic performance of Er@V_2C in the degradation of Rhodamine dye and sulfamethoxazole antibiotic.

BET analysis

Nitrogen adsorption–desorption analysis of the Er@V_2C MXene exhibited a typical type-IV isotherm with a pronounced uptake at higher relative pressures which confirmed the presence of a well-developed structure induced by erbium intercalation. The estimated Brunauer–Emmett–Teller (BET) specific surface area was approximately 90 $m^2 g^{-1}$ which indicated the effective interlayer expansion and prevention of nanosheet restacking. The total pore volume, determined near saturation pressure was around 0.45 $cm^3 g^{-1}$ reflected the formation of abundant accessible pores. The pore size distribution further revealed a dominant mesopore population centered in the range of 40–60 nm with a gradual contribution of larger pores which collectively facilitates enhanced mass transport and exposure of active sites. This hierarchical porous architecture is highly beneficial for catalytic reactions and interfacial processes contribute to improved physicochemical performance of the Er-intercalated MXene system.

3.6. Photocatalysis degradation

Significant sunlight-driven photodegradation of RhB dye and SMX antibiotic was achieved by using the catalyst Er@V_2C MXene. Figure 5a represents the time-dependent UV-Vis absorption spectra of RhB having the continuous and systematic decrease in the characteristic absorption with increasing irradiation time which confirmed the gradual breakdown of the dye molecules rather than simple adsorption [28, 29]. No significant peak shift or new absorption bands were observed that the chromophoric structure of RhB was progressively destroyed during the photocatalytic process. The corresponding degradation efficiency plot (Fig. 5b) further confirms a strong time-dependent degradation behavior with the degradation percentage increasing steadily as irradiated proceeds under sunlight. At the maximum irradiation time, the degradation efficiency reaches approximately 82.6% which demonstrated the high photocatalytic activity of the Er@V_2C composite under natural sunlight. Furthermore Fig. 5c and 5d present the photodegradation potential of Er@V_2C toward the SMX antibiotic under similar sunlight conditions. The absorption spectra of SMX showed a pronounced reduction in the characteristic UV absorption band with increasing irradiation time that indicated the effective cleavage of the aromatic and heterocyclic structures of the antibiotic. Compared to RhB, the degradation of SMX occurred more gradually which demonstrated the relatively higher chemical stability of antibiotic molecules. The degradation efficiency plot (Fig. 5d) shows a consistent time-dependent increase in degradation of SMX and demonstrated approximately 90.2% over 120 min. This higher ultimate degradation efficiency highlights the strong oxidative capability of Er@V_2C MXene toward persistent pharmaceutical pollutants.

Overall, the comparative analysis reveals that Er-intercalated V_2C MXene acts as an efficient sunlight-responsive photocatalyst for both dye and antibiotic pollutants. The different degradation rates between RhB and SMX can be attributed to their distinct molecular structures and interaction strengths with the MXene surface. In Fig. 6a, represents the temporal evolution of the concentration ratio (A_0/A) which demonstrated the progressive and accelerated degradation of both pollutants with increasing irradiation time and confirmed significant photocatalytic decomposition rather than surface adsorption. Notably, SMX exhibits a steeper increase in A_0/A compared to RhB that indicated the faster and more extensive degradation kinetics which was consistent with the higher final removal efficiency observed for SMX. This enhanced degradation of SMX reflects the strong oxidative capability of Er@V_2C toward structurally persistent pharmaceutical contaminants.

Figure 6b illustrated the pseudo-first-order kinetic plots of $\ln(A_0/A)$ versus irradiation time for RhB dye and SMX antibiotic and showed excellent linearity with high correlation coefficients which validated the degradation reactions follow first-order kinetics under sunlight irradiation. The apparent rate constant for SMX ($k = 0.009\ min^{-1}$) is higher than that for RhB ($k = 0.0061\ min^{-1}$) quantitatively confirmed the superior photocatalytic degradation rate of SMX. This kinetic enhancement was attributed to erbium induced electronic modulation of V_2C MXene which improved the visible-light absorption, promotes efficient charge separation and accelerates reactive oxygen species (ROS) generation responsible for pollutant oxidation.

The reusability and stability of the Er@V_2C photocatalyst was evaluated through consecutive degradation cycles for RhB and SMX respectively. Figure 6c represents the degradation efficiency against RhB which demonstrated only a minor decline from 82.61% in the first cycle to 79.33% after 5 cycles while for SMX (Fig. 6d) efficiency decreases slightly from 89.00% to 84.74% over the 5 cycles. This minimal performance loss (< 4% for RhB and < 5% for SMX) demonstrates excellent structural stability and resistance to photocorrosion of the Er@V_2C MXene under repeated sunlight exposure. The slight reduction in activity was likely due to partial surface fouling by reaction intermediates or minor catalyst loss during recovery rather than intrinsic material degradation.

3.7. Antioxidant activity of Er@V_2C

Figure 7a represents the antioxidant activity of Er@V_2C MXene at varying dosages, which was evaluated by using the DPPH and ABTS radical scavenging assays [30, 31]. By increasing the dosage of Er@V_2C, the scavenging efficiency was observed to be gradually increased in both DPPH and ABTS assays that reflected an enhanced electron-donating and free radical neutralization capability. At the highest concentration, the DPPH scavenging activity reached approximately 34.51 ± 0.97% while ABTS scavenging activity was around 27.44 ± 1.10%. This behavior can be attributed to the combined effects of erbium ions and surface functional groups on the MXene, which facilitate redox interactions with free radicals.

3.8. Cytotoxicity of Er@V_2C

Furthermore, the cytotoxicity of Er@V_2C MXene *in vitro* was evaluated against cervical cancer HeLa cancer cells and normal HUVEC cells and exhibited the dose-dependent behavior [32–34] as presented in Fig. 7b. At lower concentrations, Er@V_2C showed the minimal toxicity toward the normal cells which indicated the good cytocompatibility. As the concentration was increased, a progressive reduction in cell viability was observed to increase with a more pronounced effect in HeLa cells compared to HUVEC cells. This cytotoxic differential response became increasingly evident at higher doses which demonstrating the selective anticancer potential of the Er@V_2C composite. At dosage of 20 μg/mL for Er@V_2C, HeLa cell viability decreased to be approximately 39.11 ± 3.15%, whereas HUVEC cells maintained comparatively higher viability of about 51.27 ± 2.64%. This selective toxicity towards the cancer cells suggested the reduced damage to normal endothelial cells. Overall, the results indicate that Er intercalation moderates the inherent toxicity of V_2C MXene while preserving its anticancer efficacy through preferential inhibition of cancer cell growth.

Discussion

The present study demonstrates that erbium-intercalated V_2C MXene functions as a multifunctional, sunlight-responsive nanoplatform capable of simultaneously addressing environmental remediation and biomedical applications. The integration of photocatalytic, antioxidant, anticancer, and biocompatibility properties within a single MXene system highlights the effectiveness of rare-earth intercalation as a powerful strategy to modulate MXene reactivity and selectivity [35]. From the environmental perspective, the Er@V_2C MXene exhibited efficient sunlight-driven degradation of both Rhodamine B and sulfamethoxazole confirmed its ability to be functional photocatalyst under broad-spectrum solar irradiation without the need for external oxidants or artificial light sources [36]. The gradual decrease in characteristic absorption peaks and the high degradation efficiencies indicate true photocatalytic decomposition rather than simple adsorption. The superior degradation performance toward the antibiotic pollutant compared to the dye molecule highlighted the strong oxidative capacity of the system toward structurally stable and environmentally persistent contaminants. Mechanistically, erbium intercalation was expected to enhance the visible-light absorption and introduce localized energy states that facilitate efficient charge separation and reduced electron–hole recombination [37]. The photogenerated electrons and holes subsequently react with dissolved oxygen and water to generate reactive oxygen species (•OH, $•O_2^-$), which drive the oxidative cleavage of complex organic molecules. This sunlight-driven activity positions Er@V_2C MXene as a promising candidate for sustainable wastewater treatment, particularly for emerging pharmaceutical pollutants that are resistant to conventional remediation techniques [38].

Interestingly, while the Er@V_2C MXene promotes ROS generation under solar irradiation for pollutant degradation, it simultaneously exhibits concentration-dependent antioxidant activity in chemical radical scavenging systems (DPPH and ABTS) [39]. This apparent duality reflects the context-dependent redox behavior of nanomaterials. In acellular systems, surface terminations and erbium-induced electronic modulation enable electron donation and radical neutralization, whereas under photoexcitation or intracellular conditions, the same redox centers facilitate ROS generation. Such tunable redox functionality is rarely observed in conventional photocatalysts and represents a distinct advantage of MXene-based systems.

The biological studies further revealed that Er@V_2C MXene exhibits selective anticancer activity toward HeLa cells while maintaining comparatively higher viability of normal HUVEC cells, demonstrating a favorable balance between therapeutic efficacy and biocompatibility [40]. The dose-dependent cytotoxicity, with enhanced inhibition of cancer cells at higher concentrations, suggests a mechanism dominated by intracellular redox imbalance and mitochondrial dysfunction. Cancer cells are known to possess elevated basal oxidative stress and higher endocytic activity, which likely results in increased internalization of the MXene and heightened susceptibility to ROS-mediated apoptosis. In contrast, the intrinsic antioxidant capacity of Er@V_2C MXene may contribute to buffering oxidative stress in normal cells, thereby improving cytocompatibility. This selective redox modulation is particularly significant, as it addresses one of the major limitations of vanadium-based MXenes non-specific toxicity through rational rare-earth intercalation.

The coexistence of photocatalytic oxidation, antioxidant protection and selective anticancer activity within a single nanomaterial highlights the central novelty of this work. Unlike conventional photocatalysts that are typically limited to environmental applications, or biomedical nanomaterials that lack environmental functionality, Er@V_2C MXene bridges these domains through engineered electronic and surface chemistry [41]. The erbium intercalation not only stabilizes the MXene structure but also fine-tunes its redox behavior enabled the context-specific responses to light, chemical radicals and biological environments.

From a broader perspective, this study introduced the paradigm for multifunctional MXene design, where rare-earth intercalation serves as a versatile tool to simultaneously optimize photocatalytic efficiency and anticancer activity with persisting the biocompatibility. The sunlight-driven activity enhances sustainability, while selective anticancer behavior expands the scope of MXenes into therapeutic applications. Such multifunctionality is highly desirable for next-generation nanomaterials aimed at addressing interconnected challenges in environmental pollution and human health. Overall, the findings establish erbium-intercalated V_2C MXene as a novel, redox-engineered, and application-diverse nanoplatform, offering significant potential for high-impact advancements in solar-driven remediation, antioxidant systems, and cancer nanomedicine. This work not only broadens the functional landscape of MXenes but also provides critical insights into the role of rare-earth intercalation in tailoring MXene performance for complex, real-world applications.

Conclusion

Erbium-intercalated V_2C MXene was engineered (Er@V_2C) as a multifunctional adaptable sunlight-responsive nanoplatform, where the photocatalytic activity was rationally enhanced by electronic modulation of tunable biological redox activity. The successful removal of Al-layers, expansion across the layers, distortion of the lattice and stabilized erbium incorporation confirmed by structural and spectroscopic analysis showed the outline of defects stated and a reduced band-gap, drastically enhancing visible-light absorption and a separation of charge carriers. These enhanced electronically efficient properties directly converted into distinction in solar-driven photocatalytic degradation of both Rhodamine B dye and persistent antibiotic sulfamethoxazole with impartial degradation rates and preferable kinetics reported via natural sunlight, in the absence of external oxidants. Simultaneously, Er@V_2C showed redox activity with concentration dependence and selective cytotoxicity against HeLa cancer cells and relatively higher viability of normal cells of HUVEC type, which can be explained by the different redox behaviour and enhanced biocompatibility in comparison with pristine vanadium-based MXene. The bivalent capacity to facilitate the generation of reactive oxygen species to accomplish pollutant degradation and cancer cell inhibition and the radical scavenging capabilities in acellular systems highlight the exceptional importance of rare-earth intercalation in surface chemistry and electronic structure tunning MXene. Altogether, this work varieties Er@V_2C, a redox-engineered and application-diverse nanomaterial, which integrates rare earth ion intercalation as a powerful strategy for advancing of MXene-based systems towards sustainable treatment of wastewater and selective cancer nanomedicine.

Limitation and future perspectives

Despite the promising multifunctional performance of erbium-intercalated V_2C MXene, several limitations remain that warrant further investigation. The photocatalytic studies were conducted under controlled conditions using model pollutants, and the influence of complex real-water matrices, long-term stability, recyclability, and potential erbium or vanadium leaching under prolonged sunlight exposure have yet to be fully evaluated. Similarly, the biological assessments were limited to in-vitro models, and comprehensive in-vivo studies [42, 43] are required to establish biosafety, biodistribution, and therapeutic efficacy. Moreover, while redox modulation and ROS-mediated mechanisms are proposed, deeper mechanistic validation using advanced spectroscopic, molecular, and computational approaches is necessary. Future research should focus on improving structural stability, exploring surface functionalization for enhanced selectivity, extending studies to real environmental systems and multiple cancer models, and advancing toward scalable and application-oriented designs, thereby enabling the translation of rare-earth-intercalated MXenes into practical environmental and biomedical technologies.

Declarations

Author Contribution

Mahvish Fatima: Conceptualization, Methodology, Investigation, Data curation, Formal analysis, Visualization, Writing – original draft, Project administration. Majid Ali: Supervision, Conceptualization, Methodology, Validation, Writing – review & editing, Funding acquisition. Shamaila Fatima: Investigation, Formal analysis, Data curation, Validation, Writing – review & editing.Attalla F. El-kott:

Resources, Validation, Supervision, Writing – review & editing. Mohammed A. AlShehri: Resources, Formal analysis, Validation, Writing – review & editing. Eman A. Al-Shahari: Investigation, Data curation, Visualization, Writing – review & editing. Muhammad Hammad Aziz: Software, Formal analysis, Visualization, Statistical analysis, Writing – review & editing. Alisher Abduvokhidov: Supervision, Conceptualization, Resources, Funding acquisition, Project administration, Writing – review & editing.

Acknowledgement

The authors extend their appreciation to the Deanship of Research and Graduate Studies at King Khalid University for funding this work under grant number RGP.2/223/46.

References

1. Dutta S, Adhikary S, Bhattacharya S, Roy D, Chatterjee S, Chakraborty A, et al. Contamination of textile dyes in aquatic environment: Adverse impacts on aquatic ecosystem and human health, and its management using bioremediation. J Environ Manage 2024;353:120103. https://doi.org/10.1016/J.JENVMAN.2024.120103.
2. Saigl ZM. Various adsorbents for removal of rhodamine b dye: A review. Indonesian Journal of Chemistry 2021;21:1039–56. https://doi.org/10.22146/IJC.62863.
3. Imam SS, Babamale HF. A Short Review on the Removal of Rhodamine B Dye Using Agricultural Waste-Based Adsorbents. Asian Journal of Chemical Sciences 2020:25–37. https://doi.org/10.9734/AJOCS/2020/V7I119013.
4. Kumar M, Singh VP, Bhat SB, Kumar R. Environmental risks of textile dyes and photocatalytic materials for sustainable treatment: current status and future directions. Discover Environment 2025 3:1 2025;3:132-. https://doi.org/10.1007/S44274-025-00337-0.
5. Ma J, Chen Y, Zhou G, Ge H, Liu H. Recent Advances in Photocatalytic Degradation of Tetracycline Antibiotics. Catalysts 2024, Vol 14, Page 762 2024;14:762. https://doi.org/10.3390/CATAL14110762.
6. Bekele T, Alamnie G. The photocatalytic degradation of organic pollutants-a comprehensive overview. Results Chem 2025;18:102758. https://doi.org/10.1016/J.RECHEM.2025.102758.
7. Zhang DS, Wang L, Zhang X, Li XB, Xu H, Tung CH, et al. Emerging inorganic–organic hybrid photocatalysts for solar-driven overall water splitting: progress and perspectives. Chem Soc Rev 2025;54:9978–10005. https://doi.org/10.1039/D5CS00378D.
8. Ceesay E, Fatima S, Iqbal MZ, Rizwan S. Titanium Carbide (Ti3C2) Based MXenes for Energy Storage Applications. Titanium Carbide MXenes: Synthesis, Characterization, Energy and Environmental Applications 2023:207–37. https://doi.org/10.1002/9783527838707.CH10;SUBPAGE:STRING:ABSTRACT;WEBSITE:WEBSITE:PERICLES;CTYPE:STRING:BOOK.
9. Chouhan RS, Shah M, Prakashan D, Ramya PR, Kolhe P, Gandhi S. Emerging Trends and Recent Progress of MXene as a Promising 2D Material for Point of Care (POC) Diagnostics. Diagnostics 2023;13:697. https://doi.org/10.3390/DIAGNOSTICS13040697.
10. Kagalkar A, Dharaskar S, Chaudhari N. 2D-Transition Metal Carbides and Nitrides: Prospects and Challenges. ACS Symposium Series 2023;1445:1–42. https://doi.org/10.1021/BK-2023-1445.CH001.
11. Wu Y, Li X, Zhao H, Yao F, Cao J, Chen Z, et al. Recent advances in transition metal carbides and nitrides (MXenes): Characteristics, environmental remediation and challenges. Chemical Engineering Journal 2021;418. https://doi.org/10.1016/J.CEJ.2021.129296.
12. Zhou W, Sun L, Li K, Tian S. Enhanced Photocatalytic Activity of V2C MXene-Coupled ZnO Porous Nanosheets with Increased Surface Area and Effective Charge Transfer. Materials 2024, Vol 17, Page 2529 2024;17:2529. https://doi.org/10.3390/MA17112529.
13. Algaradah MM. MXene-based adsorbent materials for pollutants removal from water: Current challenges and future prospects. Inorg Chem Commun 2024;161. https://doi.org/10.1016/J.INOCHE.2024.112113.
14. Zhu S, Sun M, Mei B, Yang L, Chu Y, Shi Z, et al. Intrinsic spin shielding effect in platinum–rare-earth alloy boosts oxygen reduction activity. Natl Sci Rev 2023;10. https://doi.org/10.1093/NSR/NWAD162.
15. Shen W, Da P, Guo L, Xi P, Yan CH. Rare Earth Interface Structure Materials: Synthesis, Applications, and Mechanisms. Acc Mater Res 2024;5:712–25. https://doi.org/10.1021/ACCOUNTSMR.4C00061.
16. Al-Amiery AA, Fayad MA, Abdul Wahhab HA, Al-Azzawi WK, Mohammed JK, Majdi HS. Interfacial Engineering for Advanced Functional Materials: Surfaces, Interfaces, and Applications. Results in Engineering 2024;22. https://doi.org/10.1016/J.RINENG.2024.102125.

17. Ramezani Farani M, Mirzaee D, Hatami A, Kumar K, Ghoreishian SM, Huh YS. Biocompatibility and immunomodulation of MXenes for targeted delivery of bioactive agents and drugs. Bioact Mater 2025;55:546. https://doi.org/10.1016/J.BIOACTMAT.2025.09.038.
18. Chen L, Dai X, Feng W, Chen Y. Biomedical Applications of MXenes: From Nanomedicine to Biomaterials. Acc Mater Res 2022;3:785–98. https://doi.org/10.1021/ACCOUNTSMR.2C00025.
19. Guo J, Zhu X, Liang B, Gu X, Wu C, Li A, et al. Application and recent progress of MXene-based bioactive materials in wound management. Nano TransMed 2025;4:100079. https://doi.org/10.1016/J.NTM.2025.100079.
20. Khandelwal N, Singh N, Tiwari E, Marsac R, Schild D, Schäfer T, et al. Varying growth behavior of redox-sensitive nanoparticles on 1:1 and 2:1 clay surfaces: Mechanistic insights on preferential toxic ions removal in mono, co, and multi-metal contaminated waters. Chemical Engineering Journal 2023;461:141883. https://doi.org/10.1016/J.CEJ.2023.141883.
21. Fatima S, Sajid IH, Khan MF, Rizwan S. Synthesis and characterization of erbium decorated V2CTx for water splitting properties. Int J Hydrogen Energy 2024;55:110–7. https://doi.org/10.1016/j.ijhydene.2023.11.114.
22. Enhanced photocatalytic activity and mechanism of Ti3C2-OH/Bi2WO6:Yb3+, Tm3 + towards degradation of RhB under visible and near infrared light irradiation n.d. https://www.researchgate.net/publication/335732097_Enhanced_photocatalytic_activity_and_mechanism_of_Ti3C2-OHBi2WO6Yb3_Tm3_towards_degradation_of_RhB_under_visible_and_near_infrared_light_irradiation (accessed February 1, 2026).
23. Cheng R, Hu T, Zhang H, Wang C, Hu M, Yang J, et al. Understanding the Lithium Storage Mechanism of Ti 3 C 2 T x MXene. Journal of Physical Chemistry C 2019;123:1099–109. https://doi.org/10.1021/ACS.JPCC.8B10790/SUPPL_FILE/JP8B10790_SI_003.CIF.
24. Sun H, Song S, Xu X, Dai J, Yu J, Zhou W, et al. Recent Progress on Structurally Ordered Materials for Electrocatalysis. Adv Energy Mater 2021;11:2101937. https://doi.org/10.1002/AENM.202101937;PAGE:STRING:ARTICLE/CHAPTER.
25. Fatima S, Ali I, Abbas A, Haidry AA, Rizwan S. Er-intercalated Ti 3 C 2 T x MXene electrocatalyst for efficient energy conversion. RSC Adv 2025;15:37379–90. https://doi.org/10.1039/D5RA05111H.
26. Champagne A, Shi L, Ouisse T, Hackens B, Charlier JC. Electronic and vibrational properties of <math xmlns="http://www.w3.org/1998/Math/MathML"><msub><mi mathvariant="normal">V</mi %3E %3C mn %3E 2%3C/mn%3E%3C/msub %3E %3C mi mathvariant="normal">C%3C/mi%3E%3C/math%3E-based MXenes: From experiments to first-principles modeling. Phys Rev B 2018;97:115439. https://doi.org/10.1103/PhysRevB.97.115439.
27. Lan L, Fan X, Yu S, Gao J, Zhao C, Hao Q, et al. Flexible Two-Dimensional Vanadium Carbide MXene-Based Membranes with Ultra-Rapid Molecular Enrichment for Surface-Enhanced Raman Scattering. ACS Appl Mater Interfaces 2022;14:40427–36. https://doi.org/10.1021/ACSAMI.2C10800.
28. Kumar G, Ahlawat A, Bhardwaj H, Sahu GK, Rana PS, Solanki PR. Ultrasonication-assisted synthesis of transition metal carbide of MXene: an efficient and promising material for photocatalytic organic dyes degradation of rhodamine B and methylene blue in wastewater. Environmental Science and Pollution Research 2024 31:26 2024;31:38232–50. https://doi.org/10.1007/S11356-024-33505-5.
29. Patel R, Mahabari K, Patel K, Patel M, Jadhav AH, Dharaskar S, et al. MoS2/MXene composite material for high-performance removal of Rhodamine B dye: synthesis and application. Scientific Reports 2025 15:1 2025;15:42099-. https://doi.org/10.1038/s41598-025-26240-5.
30. Liu J, Lu W, Lu X, Zhang L, Dong H, Li Y. Versatile Ti3C2Tx MXene for free-radical scavenging. Nano Research 2021 15:3 2021;15:2558–66. https://doi.org/10.1007/S12274-021-3751-Y.
31. Jiang S, Hu D, Qi Z, Wang L, Li Y. V2CTx MXene Nanosheets as Enhanced Free-Radical Scavengers for Alleviating Oxidative Stress. ACS Appl Nano Mater 2023;6:3121–7. https://doi.org/10.1021/ACSANM.3C00391.
32. Deb VK, Yadav R, Samanta A, Kumar K, Jain U. In-Vitro Anti-cancer Therapeutic Effects of 2D-Ti3C2-MXene-Coated Hesperetin (Ti3C2_H) against Cervical Cancer Cells. Journal of Inorganic and Organometallic Polymers and Materials 2025 35:10 2025;35:8202–18. https://doi.org/10.1007/S10904-025-03750-3.
33. Scheibe B, Wychowaniec JK, Scheibe M, Peplińska B, Jarek M, Nowaczyk G, et al. Cytotoxicity Assessment of Ti–Al–C Based MAX Phases and Ti3C2Tx MXenes on Human Fibroblasts and Cervical Cancer Cells. ACS Biomater Sci Eng 2019;5:6557–69. https://doi.org/10.1021/ACSBIOMATERIALS.9B01476.
34. Huang J, Su J, Hou Z, Li J, Li Z, Zhu Z, et al. Cytocompatibility of Ti3C2Tx MXene with Red Blood Cells and Human Umbilical Vein Endothelial Cells and the Underlying Mechanisms. Chem Res Toxicol 2023;36:347–59.

https://doi.org/10.1021/ACS.CHEMRESTOX.2C00154.
35. Li H, Fan R, Zou B, Yan J, Shi Q, Guo G. Roles of MXenes in biomedical applications: recent developments and prospects. J Nanobiotechnology 2023;21. https://doi.org/10.1186/s12951-023-01809-2.
36. Kumar N, Gusain R, Sinha Ray S, editors. Two-Dimensional Materials for Environmental Applications 2023;332. https://doi.org/10.1007/978-3-031-28756-5.
37. Liu J, Ruan H, Duan P, Shao P, Zhou Y, Wang Y, et al. Photocatalytic Degradation of Antibiotics Using Nanomaterials: Mechanisms, Applications, and Future Perspectives. Nanomaterials 2025;16:49. https://doi.org/10.3390/nano16010049.
38. Jedsukontorn T, Meeyoo V, Saito N, Hunsom M. Effect of electron acceptors H2O2 and O2 on the generated reactive oxygen species 1O2 and OH· in TiO2-catalyzed photocatalytic oxidation of glycerol. Cuihua Xuebao/Chinese Journal of Catalysis 2016;37:1975–81. https://doi.org/10.1016/S1872-2067(16)62519-6.
39. Chang X, Li Z, Zhai X, Sun S, Gu D, Dong L, et al. Efficient synthesis of sunlight-driven ZnO-based heterogeneous photocatalysts. Mater Des 2016;98:324–32. https://doi.org/10.1016/j.matdes.2016.03.027.
40. Kim HS, Yi BR, Hwang KA, Kim SU, Choi KC. Anticancer Effects of the Engineered Stem Cells Transduced with Therapeutic Genes via a Selective Tumor Tropism Caused by Vascular Endothelial Growth Factor Toward HeLa Cervical Cancer Cells. Mol Cells 2013;36:347. https://doi.org/10.1007/s10059-013-0153-3.
41. Dutta T, Alam P, Mishra SK. MXenes and MXene-based composites for biomedical applications. J Mater Chem B 2025;13:4279–312. https://doi.org/10.1039/d4tb02834a.
42. Lim GP, Soon CF, Ma NL, Morsin M, Nayan N, Ahmad MK, et al. Cytotoxicity of MXene-based nanomaterials for biomedical applications: A mini review. Environ Res 2021;201:111592. https://doi.org/10.1016/J.ENVRES.2021.111592.
43. Singh B, Bahadur R, Rai D, Srivastava R. Preclinical Toxicity Assessment of Ti-Based MXene Nanomaterials for Advanced Theranostic Applications. Adv Ther (Weinh) 2024;7:2300268. https://doi.org/10.1002/ADTP.202300268;PAGEGROUP:STRING:PUBLICATION.

Figures

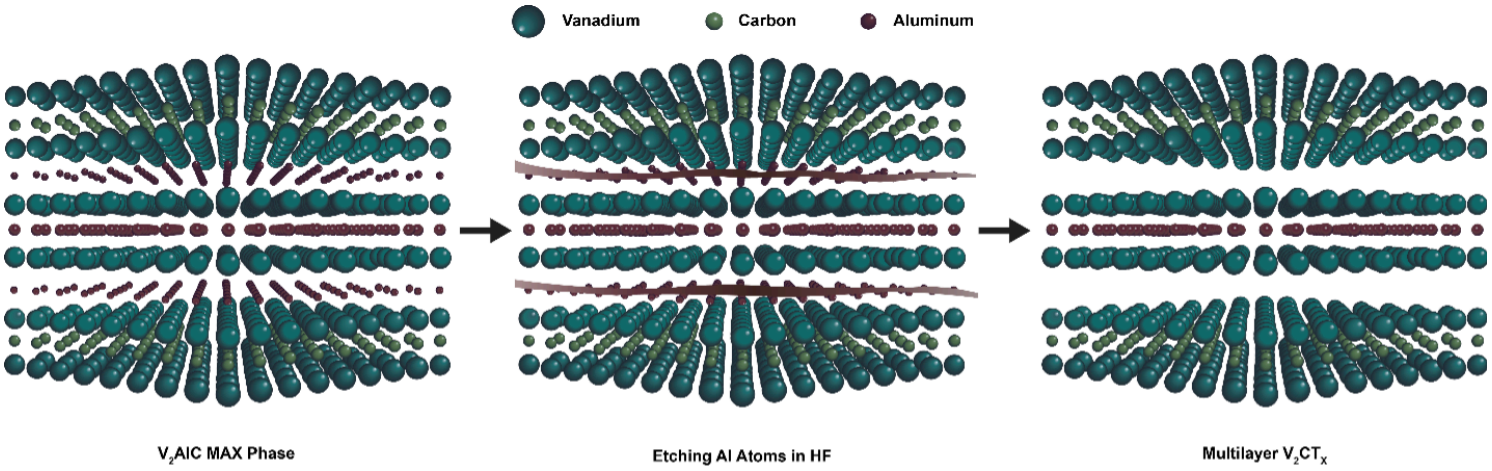


Figure 1

Schematic 1. Schematic representation of V_2AlC MAX etching and preparation of multilayered V2C MXene by Al etching.

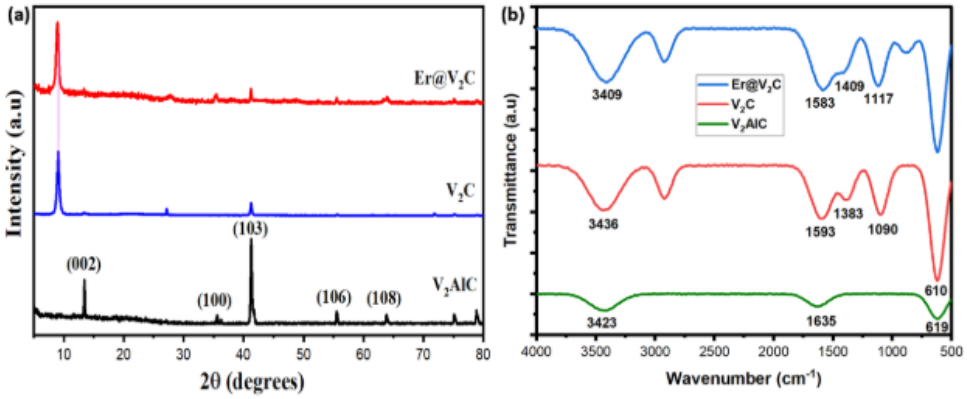


Figure 2

Represents the **(a)** XRD pattern and **(b)** FTIR spectra of V_2AlC MAX phase, V_2C MXene and Er@V_2C MXene.

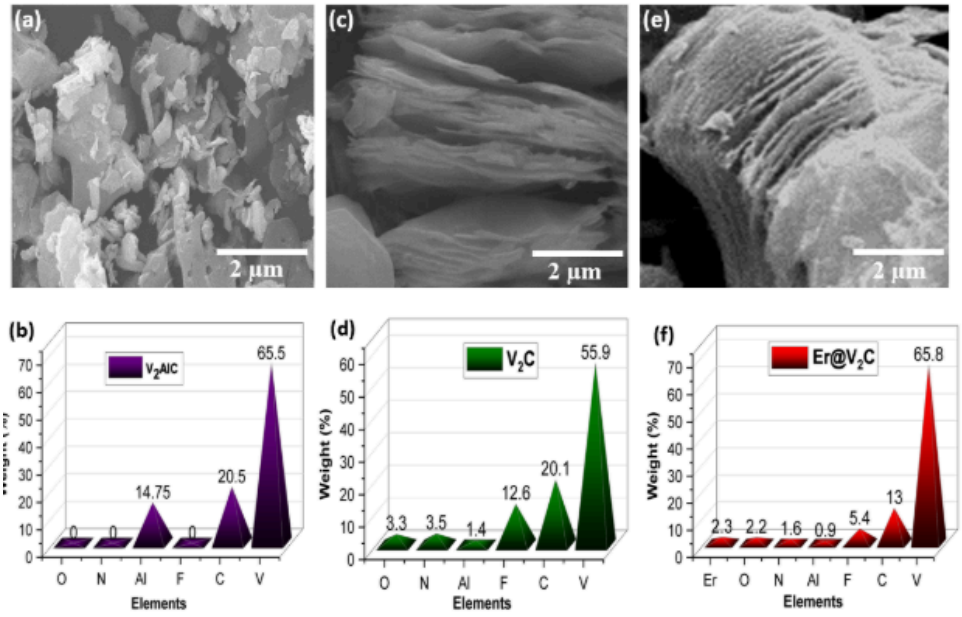


Figure 3

Represents **(a)** SEM image of V_2AlC MAX phase **(b)** wight % of elements in V_2AlC **(c)** SEM image of V_2C MXene **(d)** wight % of elements in V_2C **(e)** SEM image of Er@V_2C **(f)** weight % of elements in Er@V_2C.

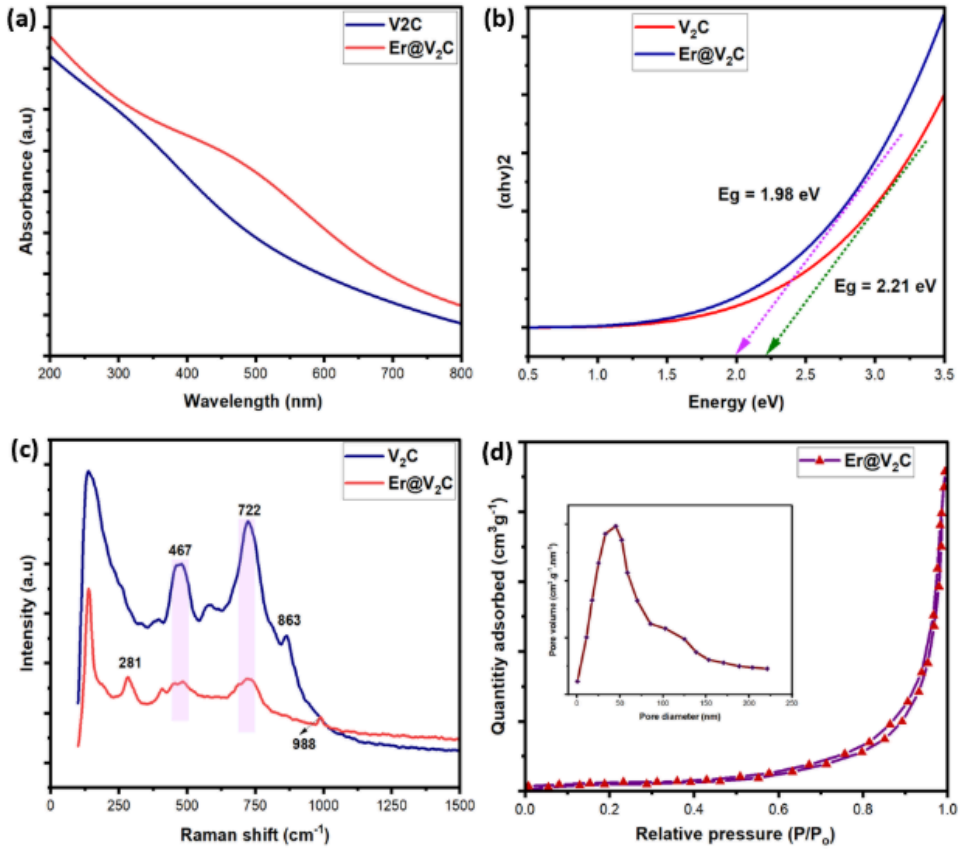


Figure 4

represents **(a)** UV-visible spectrum of V_2C and $Er@V_2C$ **(b)** Tauc plot for V_2C and $Er@V_2C$ **(c)** Raman spectra of V_2C and $Er@V_2C$ **(d)** BET analysis of $Er@V_2C$.

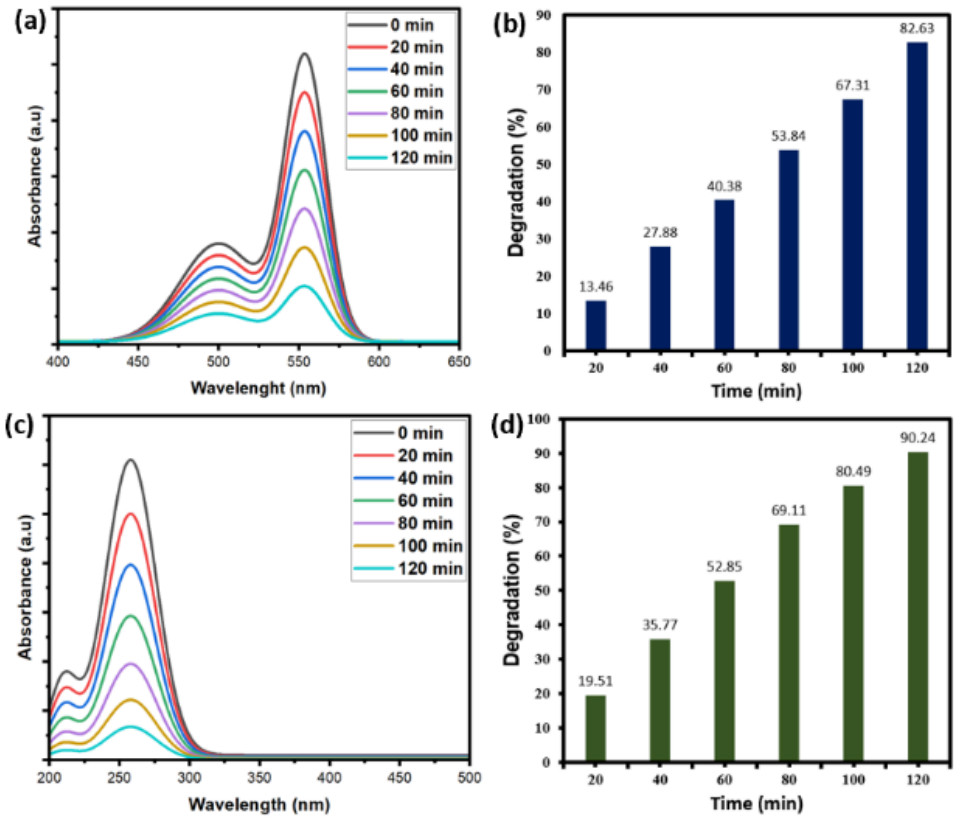


Figure 5

represents **(a)** UV visible spectra of RhB **(b)** degradation % of RhB at specific time **(c)**UV visible spectra of SMX **(d)** degradation % data of SMX at specific time.

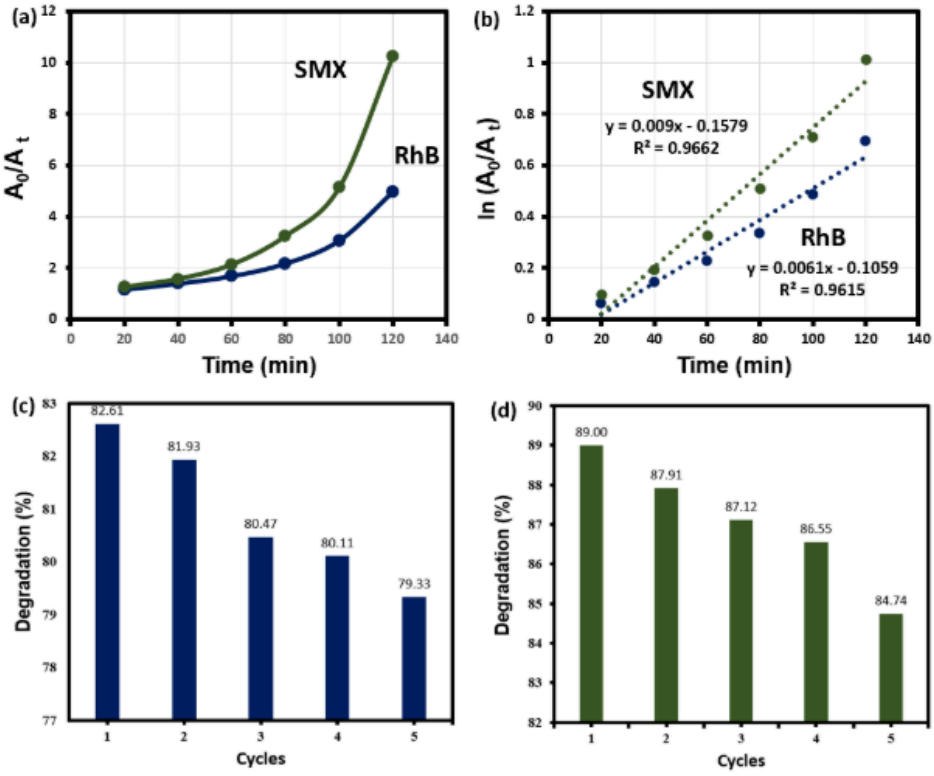


Figure 6

represents **(a)** degradation kinetics of RhB dye and SMX antibiotic **(b)** pseudo 1st order kinetics of RhB dye and SMX dye **(c)** degradation cycles for RhB dye **(d)** degradation cycles for SMX antibiotic

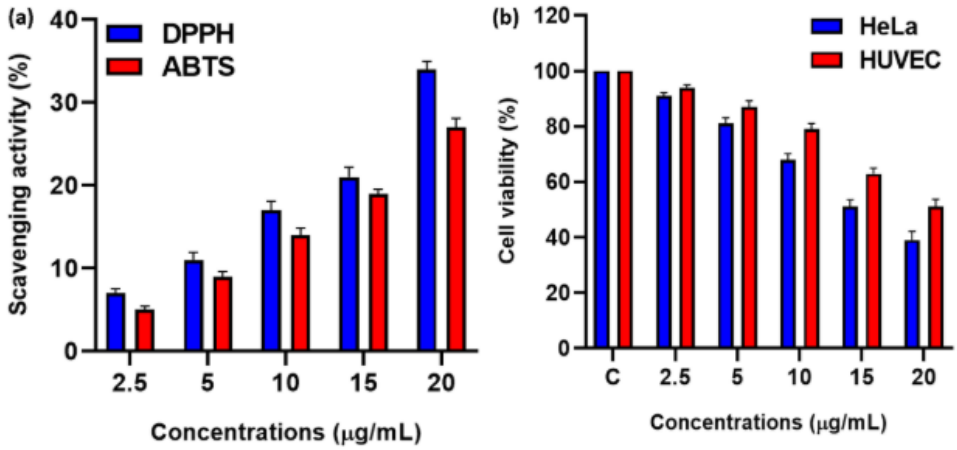


Figure 7

Represents **(a)** antioxidant activity of Er@V_2C MXene assessed by DPPH and ABTS assays **(b)** Er@V_2C cytotoxicity against cancerous cervical HeLa and normal HUVEC cell lines at varying concentrations.